Learning generative models for geostatistical facies simulation based on a single training image

Runhai Feng[1]*, Dario Grana[2]

[1]Aramco Research Center - Beijing, Aramco Asia, Beijing, China

[2] School of Energy Resources, University of Wyoming, Laramie, WY, USA

* Corresponding author. Email: runhai.feng@aramcoasia.com

Abstract

Characterization of subsurface reservoirs often requires geological facies models to identify areas with favorable rock properties. With the development of computing powers, deep learning approaches, such as the generative adversarial networks (GANs), became widely used for simulating complex geological models. However, training of the GANs typically requires a large quantity of training data for updating neural parameters. This process is generally done using traditional geostatistical methods based on multiple-point statistics or process-based models to build the training data. In this study, we propose to train the GANs using one single training image, a conceptual model from which the statistics of the geological patterns can be extracted. The training image is first down-sampled to different scales, and the generator and the discriminator are trained alternately for each scale. The training process is implemented from the coarsest to the finest scale to learn the spatial statistics from the training image progressively. We apply the proposed GANs to simulate the 2D Lena river delta and 3D Descalvado aquifer analog model, in which complex geological patterns and structures from the training image are successfully learned and reproduced by GANs. The gradual deformation method is further applied to iteratively calibrate the random realizations by the generator to

observed data, in an optimization workflow. The optimization scheme is implemented many times to obtain multiple independent models that all match the observed data.

Keywords: Training image; GANs; Geostatistical simulations; Multiple scales; Model calibration

1 Introduction

Geological facies modelling consists in generating spatial models in two- or three-dimensions of a categorical variables representing the spatial distribution of geological facies or rock types with realistic geological patterns. These models are commonly used in groundwater, carbon storage, and hydrocarbons exploration studies to identify geo-bodies with rock and fluid properties of interest. Many geostatistical approaches for facies modelling have been proposed such as two-point statistics, multiple-point statistics, object-based and process-based methods (Strebelle, 2002; Hu and Chugunova, 2008; Mariethoz et al., 2010; Mariethoz and Caers, 2014; Pyrcz and Deutsch, 2014). In recent years, deep learning methods have been applied for geostatistical modeling of categorical and continuous variables such as facies or rock and fluid properties. Various generative models have been trained to reproduce the complex geometrical patterns representing realistic realizations of the spatial distribution of geological facies. One of the most popular methods is the generative adversarial networks (GANs) (Goodfellow et al., 2014), which can generate realistic models and have been widely used in geoscience applications (Dupont et al., 2018; Chan and Elsheikh, 2019; Azevedo et al., 2020). Laloy et al. (2018) use GANs to generate two- and three-dimensional geological facies models in an unconditional way. Sun (2018) presents a state-parameter identification GAN for learning bidirectional relations between parameter space and corresponding model space. Chen et al. (2022) model subsurface sedimentary facies using an advanced self-attention GAN to capture and reproduce large scale features of the training image. Feng et al. (2022) investigate GANs within the Bayesian framework for geological facies modelling.

The application of GANs in facies modelling has also been extended to conditional simulation, in which random realizations are constrained to physical measurements (i.e. direct observations). The conditional simulation by GANs can be treated as a semantic image inpainting problem, in which the task to generate constrained models is formulated as an optimization problem (Yeh et al., 2017). The optimization process can be divided into two steps (Zhang et al., 2021), to train unconditional GANs for producing plausible facies models when inputting latent vectors (step 1) and to update the location of the input vectors in the latent space based on the computed error between generated model and conditioning data (step 2). Mosser et al. (2018) apply the content loss for constraining the conditioning data and generate conditional pore and reservoir-scale models. Zhang et al. (2019) use GANs to learn the sedimentary architecture and simulate geologically realistic three-dimensional reservoir facies models. Zhong et al. (2019) formulate conditional GANs to learn the dynamic functional mappings in multiphase models and predict the CO2 plume migration in heterogeneous storage reservoirs. In contrast to the two-step approach (Yeh et al., 2017), Zhang et al. (2021) propose to perform the conditioning of facies models in the training process of GANs, adopting the idea of image-to-image translation (Isola et al., 2018). The progressive growing of GANs has been applied by Song et al. (2021) for conditioning geophysics-interpreted probability maps, and multiple geological facies models are generated, which are consistent with input conditions.

However, in the aforementioned studies, a large quantity of training data is typically required to update neural parameters of GANs in the training process, and some traditional geostatistical methods are commonly applied to generate such training data (e.g. Song et al., 2021; Zhang et al., 2021; Feng et al., 2022; Sun et al., 2022). Therefore, the training of GANs models heavily relies on the geostatistical methods, even though the trained GANs can reproduce complex geological patterns more computationally efficiently. In order to address this problem, we propose to train the GANs model based on a single training image, without using any geostatistical method for building the training data. The proposed GANs perform unconditional simulations based on a multi-scale architecture (Shocher et al., 2018; Shaham et al., 2019). Moreover, we apply the gradual deformation method (GDM) with an optimization workflow to iteratively calibrate the random realizations generated by GANs to the observed data (Hu, 2000; Caers, 2007). The novelty of the proposed method is that the training of GANs only uses one single training image according to the simulation approach used in multiple-point statistics (MPS); in addition, the proposed method does not require the stationary assumption of the training image. The proposed GANs model is applied to simulate complex 2D river delta and 3D geochemical facies models, and the random realizations are then conditioned/calibrated to honor observed data using GDM.

2 Methodology

2.1 GANs based on a single training image

GANs are networks consisting of two components: the discriminator (D) and the generator (G). During the training process, the generator tries to generate images as realistic as possible, while the discriminator aims to distinguish the real images from the fake ones (Goodfellow et al., 2014). The training process of GANs is iteratively implemented. Once trained, the generator of GANs is given with latent vectors that are drawn from a pre-defined distribution, and plausible and diverse models are generated to reproduce the probability distribution of the training data (Zhang et al., 2021).

In this work, in the context of geological facies modeling, instead of using multiple training images as the training data, we only use one single training image for updating neural parameters of GANs. This is achieved by introducing a pyramid of fully convolutional GANs, where each is responsible for capturing the spatial statistical distribution of down-sampled patches of the training image at different scales (Shaham et al., 2019). Figure 1 shows the high-level architecture of the proposed GANs, consisting of a pyramid of generators and discriminators to be trained at different scales (Shaham et al., 2019). The single training image x is first down-sampled to different scales by a factor of r, making the image pyramid of $\{x_0, \cdots x_n, \cdots, x_N\}$. The final image x_N has the same size of the image x. Correspondingly, the proposed GANs model has a pyramid of generators $\{G_0, \cdots G_n, \cdots, G_N\}$ and discriminators $\{D_0, \cdots D_n, \cdots, D_N\}$, which are trained with the down-sampled image patches individually (Fig. 1).

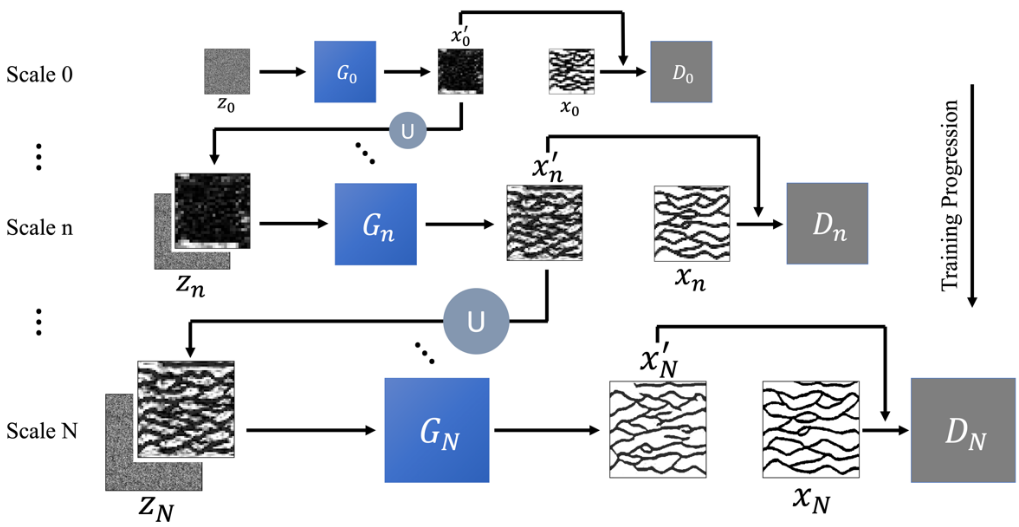

Fig. 1 Schematic view of the multi-scale architecture of GANs where the training of the generator and discriminator is performed from the coarse to the fine scale (Scale 0 to Scale N). U stands for the up-sampling operation.

All the generators and discriminators are trained sequentially, starting from Scale 0 (Fig. 1), and once G_n and D_n are trained, they are kept fixed, and the training process is moved to the next scale level. The generation process at the n^{th} level involves all the generators $\{G_0, \cdots, G_n\}$, as well as the random noise maps $\{z_0, \cdots, z_n\}$ up to the current level (Shaham et al., 2019). At the n^{th} scale level, an adversarial training process is performed separately: the generator G_n tries to generate fake image x'_n to fool the discriminator D_n and the discriminator D_n attempts to distinguish the real image x_n from the fake one x'_n. Different from other GANs where the 1D latent vectors are considered as inputs, in the proposed implementation, the generator G_n here takes an image sample generated by the up-sampled trained generator at the previous scale x'_{n-1} and the 2D random noise map z_n as inputs.

At the coarsest scale (Scale 0 in Fig. 1), there is no image sample, and only the random noise map z_0 is given to the generator G_0 for generating an image sample x'_0. Each generator G_n is trained to learn the internal structure of the training image at different scales, and the finer details from the training image are learned sequentially, as the finer scale details cannot be generated by the previous generators $\{G_0, \cdots, G_{n-1}\}$. Indeed, this multi-scale strategy is similar to the multiple grid simulation approach used in MPS methods for capturing large scale structures of geological models of interest (Tran, 1994). The formulation for generating an image sample at the n^{th} level is given by:

$$x'_n = \begin{cases} G_0(z_0) & n = 0 \\ G_n(z_n, (x'_{n-1}) \uparrow) & 0 < n \leq N \end{cases} \tag{1}$$

in which $\uparrow$ represents the up-sampling operation (U in Fig. 1).

The loss function at the n^{th} scale level for G_n and D_n is formulated as (Shaham et al., 2019):

$$\min_{G_n} \max_{D_n} \mathcal{L}(G_n, D_n) = \mathcal{L}_{adv}(G_n, D_n) + \alpha \mathcal{L}_{rec}(G_n), \tag{2}$$

where $\mathcal{L}_{adv}$ is the adversarial loss used in common GANs training for penalizing the distribution distance between down-sampled image x_n and generated image sample x'_n; α is a weighting factor to balance the two loss functions; and $\mathcal{L}_{rec}$ is the reconstruction loss to ensure that x_n can be reproduced given a specific set of random noise maps. A random noise map z^* is drawn once at the coarsest level (Scale 0, Fig. 1) and is kept fixed in the training process afterwards. The reconstructed image at the n^{th} scale is denoted as x_n^{rec}, and the reconstruction loss function is given by:

$$\mathcal{L}_{rec} = \|x_n^{rec} - x_n\|^2, \;\; 0 \leq n \leq N \tag{3}$$

where x_n^{rec} can be generated as:

$$x_n^{rec} = \begin{cases} G_0(z^*) & n = 0 \\ G_n(0, (x_{n-1}^{rec}) \uparrow) & 0 < n \leq N \end{cases} \tag{4}$$

The deep convolutional neural networks are applied to design the generators and discriminators at different scales using PyTorch, and they all have the same network architecture. Figure 2 shows the neural network architecture for the generator and discriminator. At the n^{th} scale level, the image sample generated by the generator from the previous scale x'_{n-1} is first up-sampled to the current resolution and added to the random noise map z_n. This result is then considered as the input to the convolutional block with 5 layers. The output from the last convolutional layer is added with the up-sampled x'_{n-1} to obtain x'_n. The first four convolutional layers in the ConvBlock (Fig. 2a) have 32 kernels whereas only 1 kernel is used in the last convolutional layer. The kernel size for the two-dimensional filters is 3×3, with a stride step of 1×1. Each convolutional layer is followed by a batch normalization (Ioffe and Szegedy, 2015), and the Leaky rectified linear unit (ReLU) is used as the activation function, except in the last layer where the hyperbolic tangent (tanh) function is applied (Fig. 2a). The discriminator D_n at the n^{th} scale has a similar network architecture with the generator G_n (Fig. 2b), for distinguishing between the generated fake image x'_n and real image x_n down-sampled to the current resolution. Moreover, a Markovian discriminator (Li and Wand, 2016) is applied to classify the input as real or fake, by calculating the mean of the patch output from the last convolutional layer of D_n. The number of kernels in the ConvBlock for the generator and discriminator (Fig. 2) is increased by a factor of 2 for every 4 scales, in order to capture more details at the finer scale.

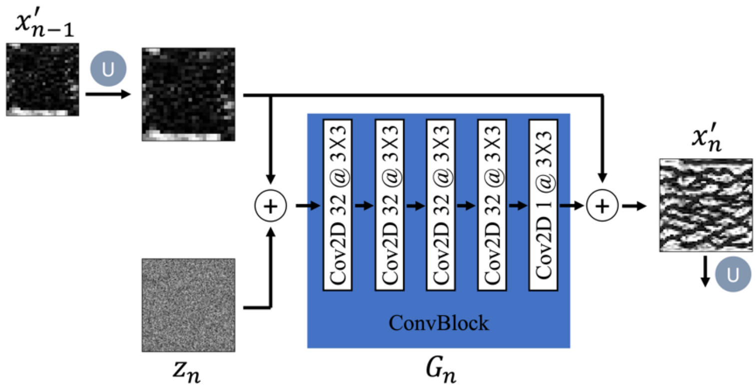

(a)

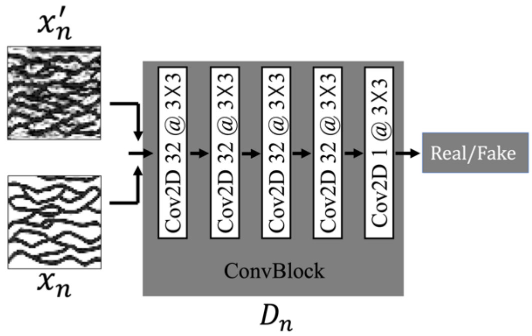

(b)

Fig. 2 Network architecture for the generator (a) and discriminator (b) at the n^{th} scale level.

The number of training epoch is 2,000 to train each generator and discriminator per scale, with a learning rate of 0.0005 and the Adam optimizer (Kingma and Ba, 2014). The hyperparameter α (Eq. 2) is set as 10 to weight the loss contribution between $\mathcal{L}_{adv}$ and $\mathcal{L}_{rec}$. The total scale number N for the multi-scale training as well as for down-sampling the training image (Fig. 1) is determined by the scale factor r and original size of the training image:

$$N = \text{ceil}\left[\log_r\left(\frac{25}{\text{min (size of image)}}\right)\right] + 1, \tag{5}$$

where the function of ceil rounds a real number to the nearest integer, the min function returns the lowest value of the size of the image, and r is the scale factor assumed to be 0.75.

2.2 Data calibration/conditioning using gradual deformation method

The presented GANs can only generate random realizations, without any data conditioning/calibration. Then, the gradual deformation method (GDM) is applied to condition/calibrate the GANs random realizations to observed data **d** as a result of an optimization problem where the realizations are stochastically perturbed until they match the data **d** (Hu, 2000; Hu et al., 2001; 2004). The principle of GDM is to generate perturbations of initial model realizations in such a way that the realizations match the observed data at the data locations (Caers, 2007). Given two independent Gaussian functions $\mathbf{Y}_1$ and $\mathbf{Y}_2$, a Gaussian random function $\mathbf{Y}$ is built as a linear combination of $\mathbf{Y}_1$ and $\mathbf{Y}_2$ as

$$\mathbf{Y}(\theta) = \mathbf{Y}_1 \cos\theta + \mathbf{Y}_2 \sin\theta, \tag{6}$$

with θ being the perturbation parameter (Hu, 2000). When $\theta = 0$, then $\mathbf{Y} = \mathbf{Y}_1$; and when θ is gradually increased to $\pi/2$, $\mathbf{Y} = \mathbf{Y}_2$. Given two independent realizations $\mathbf{y}_1$ and $\mathbf{y}_2$ of $\mathbf{Y}_1$ and $\mathbf{Y}_2$, then $\mathbf{y}(\theta)$ represents a set of realizations:

$$\mathbf{y}(\theta) = \mathbf{y}_1 \cos\theta + \mathbf{y}_2 \sin\theta, \tag{7}$$

Consider $\mathbf{y}$ a realization of $\mathbf{Y}$ and $\mathbf{g}$ the forward operator that relates $\mathbf{y}$ to $\mathbf{d}$, then an objective function $\mathcal{L}$ can be formulated in the optimization process for finding model parameters $\mathbf{y}$ to match observed data $\mathbf{d}$:

$$\mathcal{L} = \|\mathbf{d} - \mathbf{g}(\mathbf{y})\|, \tag{8}$$

and minimizing the difference between the observed data $\mathbf{d}$ and the simulated data $\mathbf{g}(\mathbf{y})$. When $\mathbf{y}$ is parameterized with the perturbation parameter θ, then $\mathcal{L}$ in Eq. (8) becomes a function of θ:

$$\mathcal{L}(\theta) = \|\mathbf{d} - \mathbf{g}(\mathbf{y}(\theta))\|, \tag{9}$$

and the multi-dimensional optimization problem in Eq. 8 becomes a one-dimensional optimization problem (Eq. 9), to find the optimal value of the perturbation parameter θ^{opt} such that $\mathbf{g}(\mathbf{y}(\theta^{opt}))$ best matches $\mathbf{d}$ (Caers, 2007).

In practice, a single optimization of θ could not result in a model that matches $\mathbf{d}$ satisfactorily, and a repeated workflow is required by generating new realizations and repeating the optimization in an iterative procedure (Caers, 2007):

1. Generate two independent Gaussian realizations $\mathbf{y}_1$ and $\mathbf{y}_2$
2. Iterate until the observed data $\mathbf{d}$ are matched
    - Search θ in a range between 0 and $\pi/2$ for optimization

$$\theta^{opt} = \min_{\theta}\{\mathcal{L}(\theta) = \|\mathbf{d} - \mathbf{g}(\mathbf{y}_1 \cos\theta + \mathbf{y}_2 \sin\theta)\|\}, \tag{10}$$

    - Set (i) $\mathbf{y}_1 = \mathbf{y}(\theta^{opt})$

      (ii) Generate a new random realization $\mathbf{y}_{\text{new}}$

      (iii) $\mathbf{y}_2 = \mathbf{y}_{\text{new}}$

For obtaining N_c conditional/calibrated realizations, the workflow is implemented N_c times.

3 Application

3.1 Two-dimensional Lena river delta

The first example for the facies simulation by the proposed GANs is a complex fluvial model from the Lena river delta (Hu et al., 2014). The training image represents the spatial distribution of facies derived from a satellite image (Fig. 3) with a cutoff operation on the digital values (http://earthobservatory.nasa.gov/IOTD/view.php?id=2704).

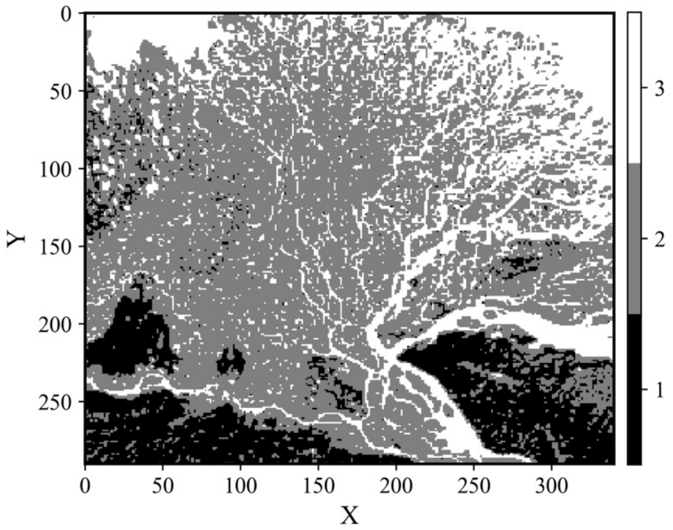

Fig. 3 Training image of the 2D Lena river delta.

The original training image with a pixel size of 340 × 290 is then down-sampled to different scales (Eq. 5). Fig. 4 shows the image pyramid of $\{x_0, \cdots x_5, \cdots, x_9\}$ from the coarsest to the finest scale. In total, there are 11 scales, and the training image at the original resolution (Fig. 3) is considered as x_{10}.

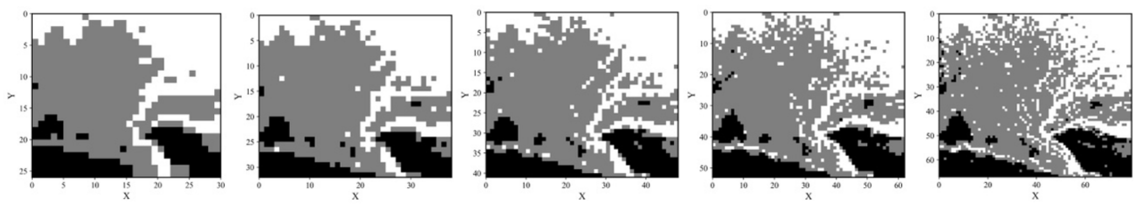

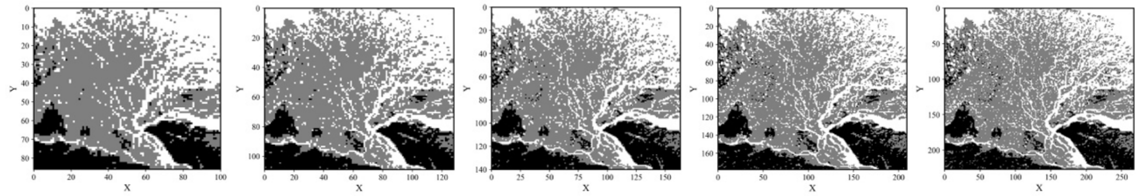

Fig. 4 The pyramid of training image that has been down-sampled to different scales $\{x_0, \cdots x_5, \cdots, x_9\}$.

These down-samples images (Fig. 4) are used as training data for updating the GANs at each scale (Fig. 1), and the total training time is about 2 hours using the GPU of NVIDIA Quadro RTX 6000. The trained generator is then used to randomly generate 100 facies models, which only takes approximately 10 s. Figure 5 shows six randomly selected realizations of the 2D Lena river delta, and all of them can successfully capture the geometry of the river delta with diverse variations.

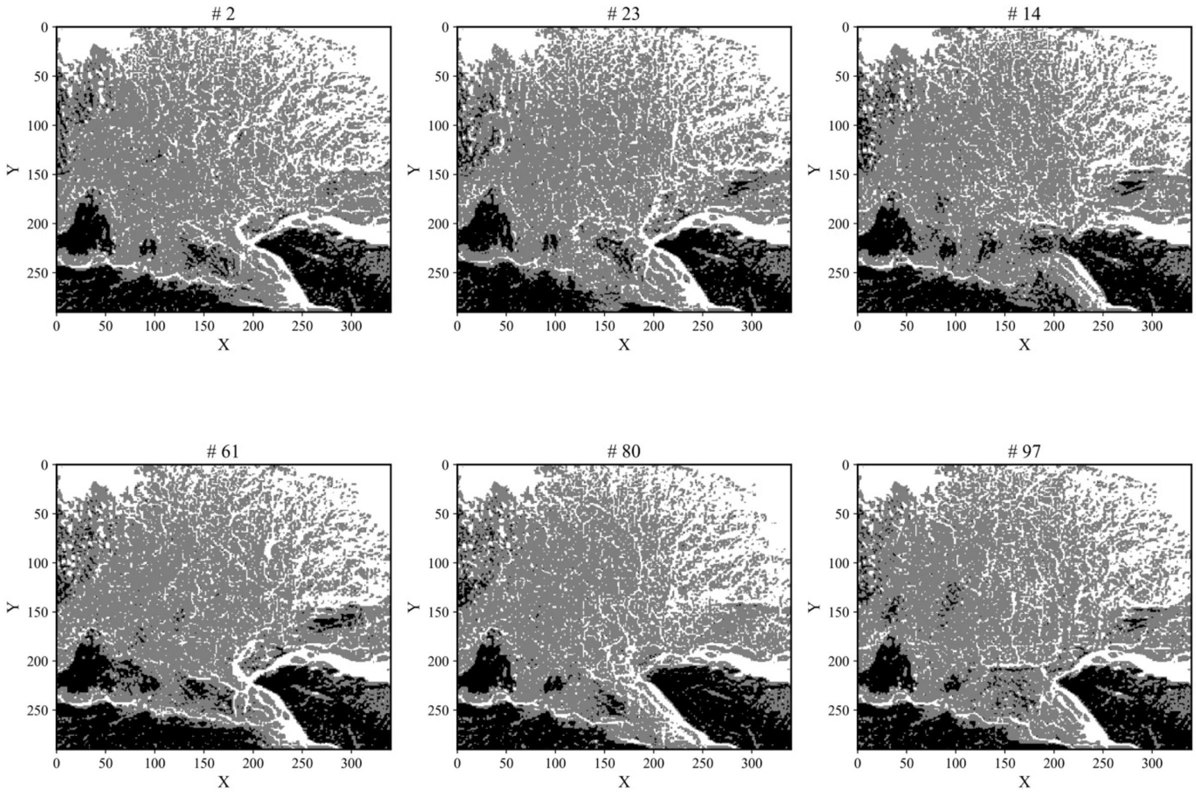

Fig. 5 Six randomly selected realizations of the Lena river delta by the trained GANs.

Furthermore, by changing the input size of the random noise map, the trained GANs are able to generate realizations of any arbitrary image size, as the full convolutional layers are used in the generator (Shaham et al., 2019). Figure 6 shows the random realizations for different image sizes, and all of them show similarities with the training image (Fig. 3).

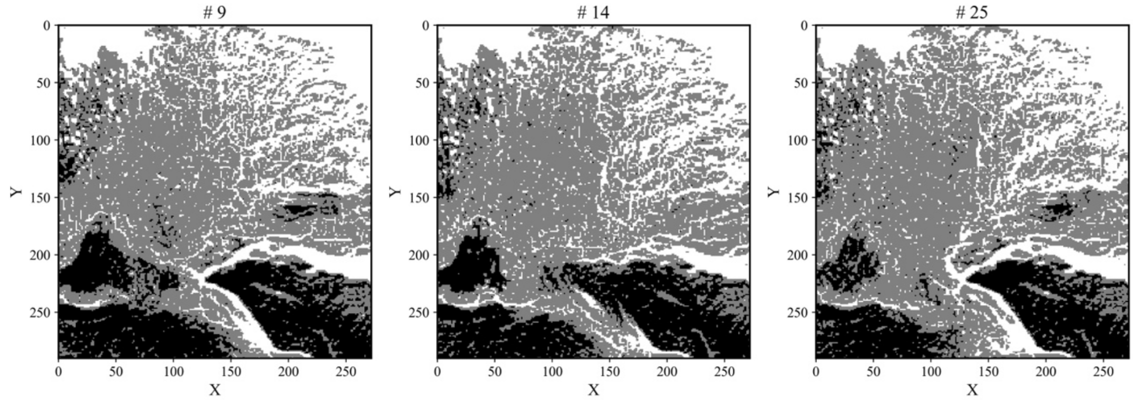

(a)

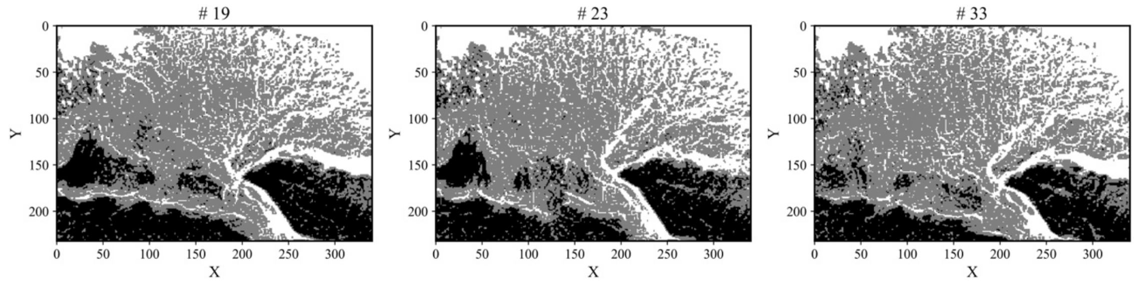

(b)

Fig. 6 Random realizations of image size of 272×290 (a) and 340×232 (b).

The randomly generated realizations do not honor any observed data, and the proposed GDM is then used to condition/calibrate these models to observational data. Within the multi-scale architecture of GANs, the random noise maps are drawn independently from a pre-defined Gaussian distribution and are kept at each scale. The generation of the facies model by the trained GANs is considered as the forward operator **g** in the optimization problem (Eq. 10), based on a linear perturbation of the random noise maps at each scale (Fig. 2a). A gradual deformation of the facies models between two random realizations is shown in Fig. 7, in which the facies models are gradually perturbed from $\theta = 0$ to $\theta = \pi/2$.

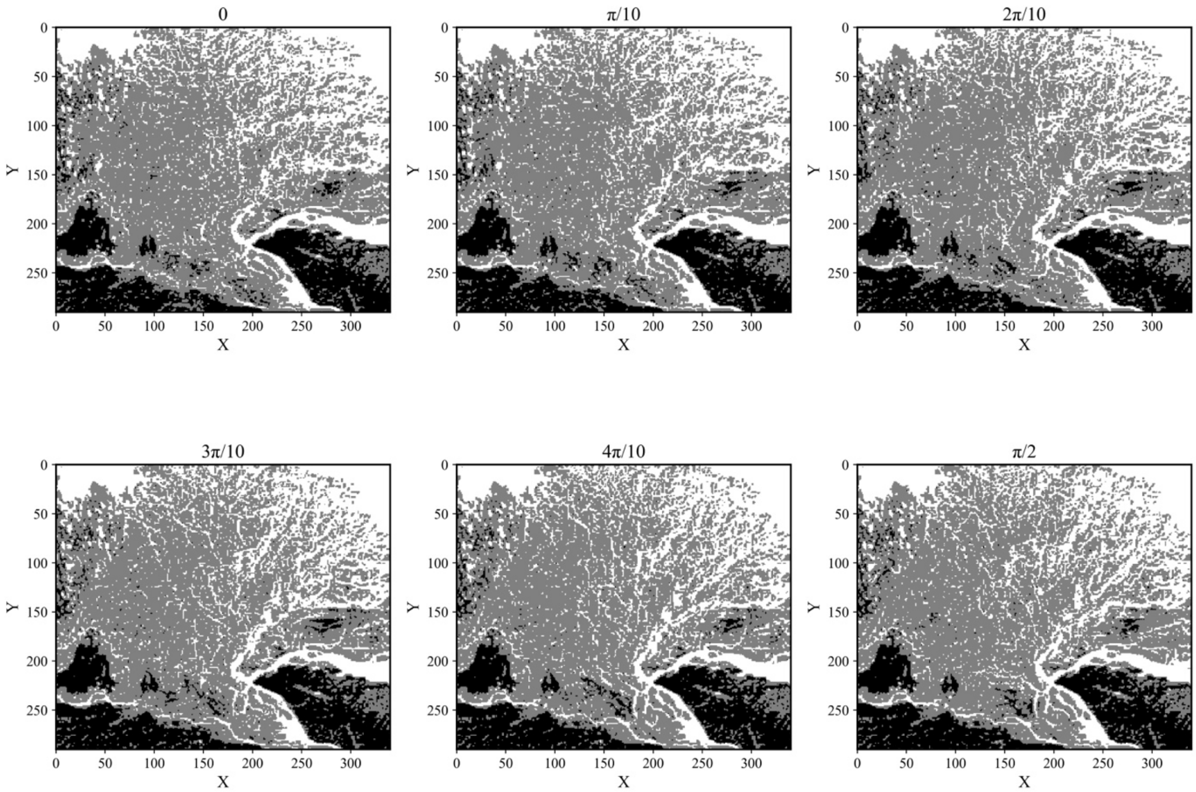

Fig. 7 Gradual deformation between two random realizations of facies models ($\theta = 0$ and $\theta = \pi/2$).

The conditional/calibrated facies models by the GDM are shown in Fig.8, where the red circles represent the locations where the channel facies (white color) are observed (Fig. 8). Compared to the unconditional realizations (Fig. 5), the conditional/calibrated realizations better capture the channel structures based on the observed data.

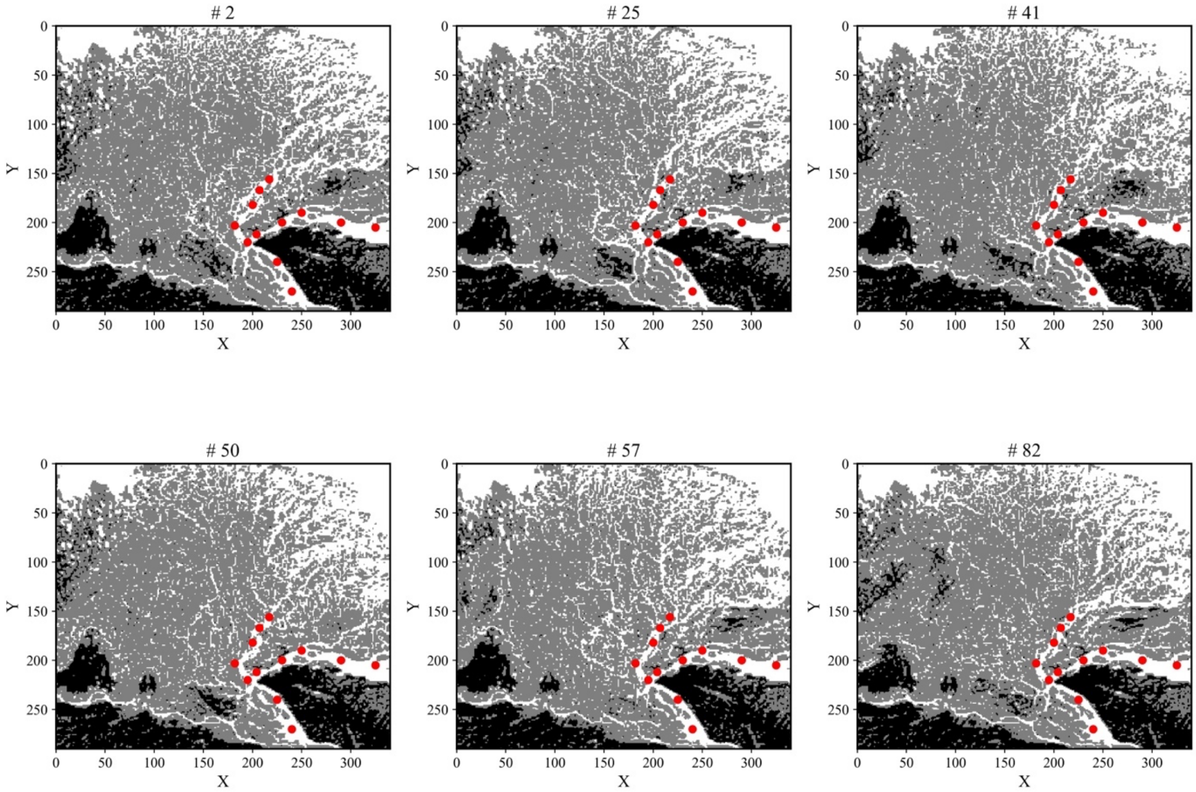

Fig. 8 Six conditional/calibrated facies models by the proposed GDM to observed channel facies (red circles).

Figure 9 shows the entropy values based on 100 unconditional realizations and conditional realizations, respectively. When constrained to the channel facies hard data, the channel geometry shows smaller entropy values (Fig. 9b, red arrows), which means that the channel facies are simulated consistently with the observed data, compared to the unconditional realizations (Fig. 9a, red arrows). The discontinuous artifacts in Fig. 9 are due to the 2D convolutional filters used and the limited local variability of the facies distribution in the training image at some areas.

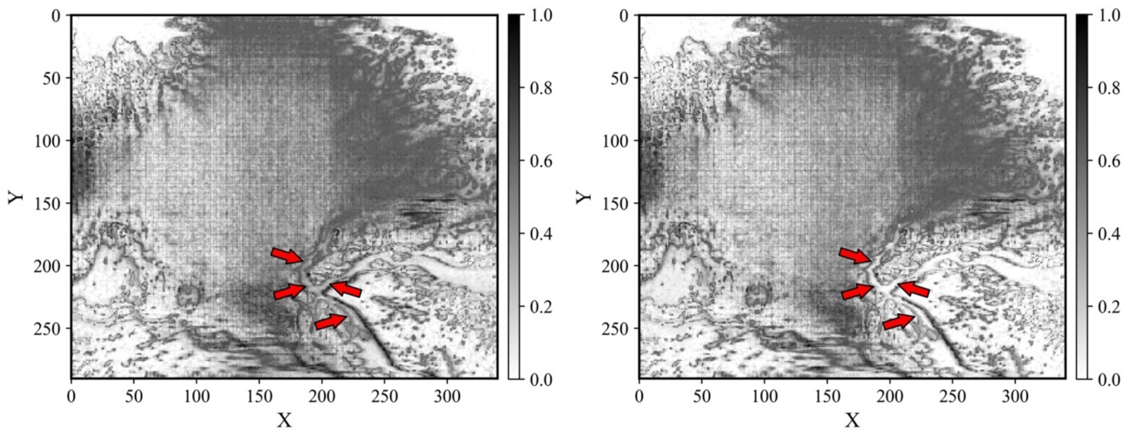

(a) (b)

Fig. 9 Entropy values based on 100 unconditional realizations (a) and 100 conditional realizations (b). Darker color represents larger uncertainty for the facies simulation.

To compare their spatial variability, the training image, unconditional/random realizations and conditional/calibrated realizations are mapped into a low-dimensional space using multi-dimensional scaling (MDS) with Euclidean distance (Cox and Cox, 2008). Unconditional/random realizations and conditional/calibrated realizations overlap with the training image quite well in the 2D space, meaning that there is a good similarity with the training image (Fig. 10). Furthermore, unconditional/random realizations and conditional/calibrated realizations are scattered well in the 2D space, indicating a large diversity among them.

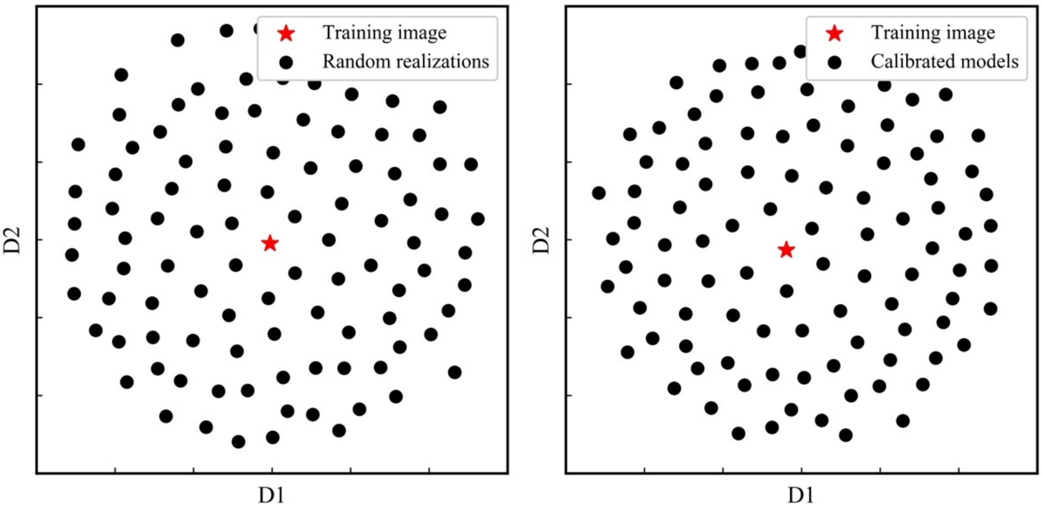

(a) (b)

Fig. 10 MDS plot of the training image with unconditional/random realizations (a) and conditional/calibrated models (b).

The facies proportions are shown in Fig. 11, in which the unconditional/random realizations and conditional/calibrated realizations can successfully reproduce the histogram of the three facies in the training image.

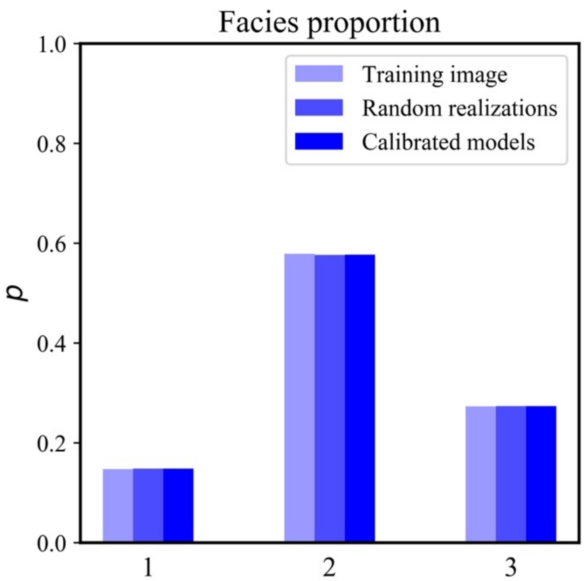

Fig. 11 Facies proportions of training image, random realizations and calibrated models.

3.2 Three-dimensional Descalvado aquifer analog

The second example for the proposed method is the 3D Descalvado aquifer analog data for characterizing sedimentary structures to analyze groundwater formations in Brazil (Bayer et al., 2015). The original nine facies have been merged into four facies, based on the similarity of grain size, sorting and texture. Fig. 12 shows the training image of the analog dataset in 3D space and slices for inspecting internal structures. The pixel size of the 3D facies model is $250 \times 50 \times 50$ in the X-, Y- and Z-directions.

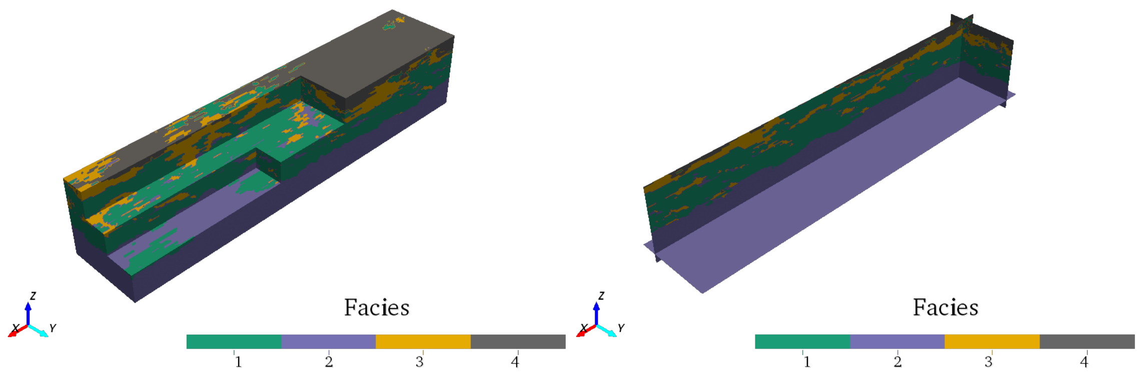

(a) (b)

Fig. 12 Training image of the Descalvado analog dataset in 3D space (a) and slices (b). 1: Trough-cross-bedded sand and gravel; 2: Planar-cross-bedded aeolian sand; 3: Horizontally-laminated to planar cross-stratified sand; 4: Trough-cross-bedded sand and clay intraclasts.

The training image in Fig. 12 is then down-sampled to different scales (Eq. 5) for training the proposed GANs (Fig. 1), in which the convolutional kernels are extended to 3D accordingly. The hyperparameters such as training epoch, learning rate, and number of hidden layers are the same with the ones used in the 2D case study. It takes about 12 hours for training the multi-scale GANs, and approximately 60 s for generating 100 unconditional realizations. Figure 13 displays three randomly selected realizations by the trained GANs, showing a similar structure with the training image (Fig. 12)

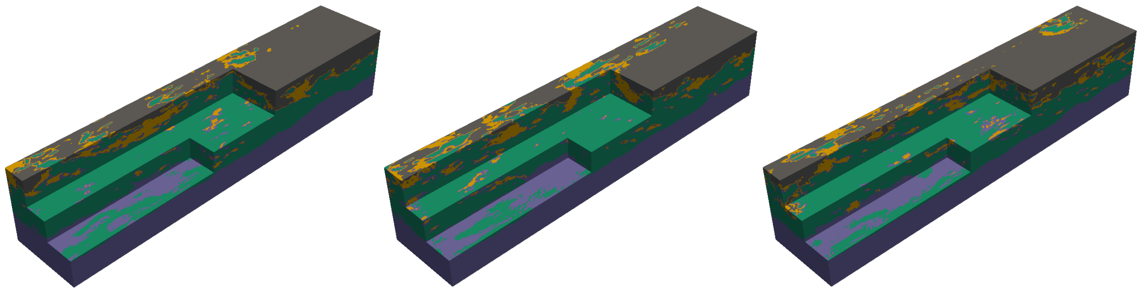

(a)

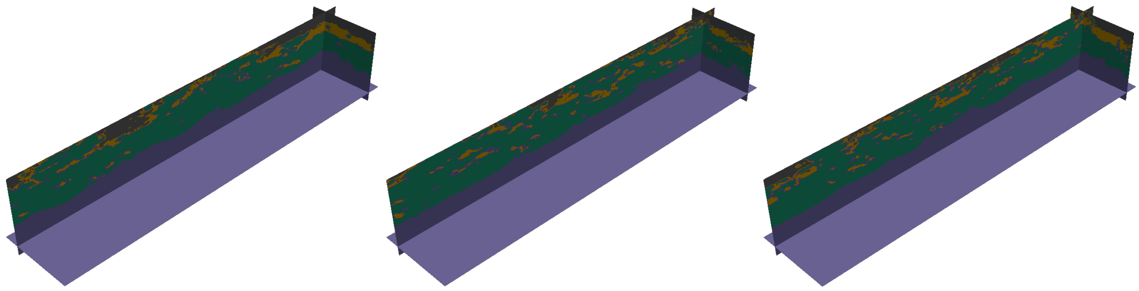

(b)

Fig. 13 Three randomly selected realizations in 3D space (a) and their corresponding slices (b).

The proposed GDM is then applied to condition/calibrate the random realizations to observed data. The data consists of a pseudo well with known facies distribution at the location $X = 126$ and $Y = 26$. Figure 14 shows three conditional/calibrated realizations, together with the training image and three selected unconditional/random realizations of the cross section at $X = 126$. After data conditioning/calibration, the facies at the well location (Fig. 14, red line) are reproduced in the conditional/calibrated realizations (Fig. 14c), compared to the unconditional/random realizations (Fig. 14b).

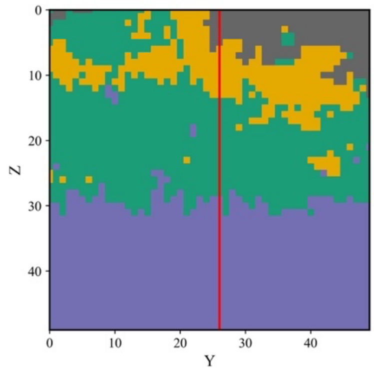

(a)

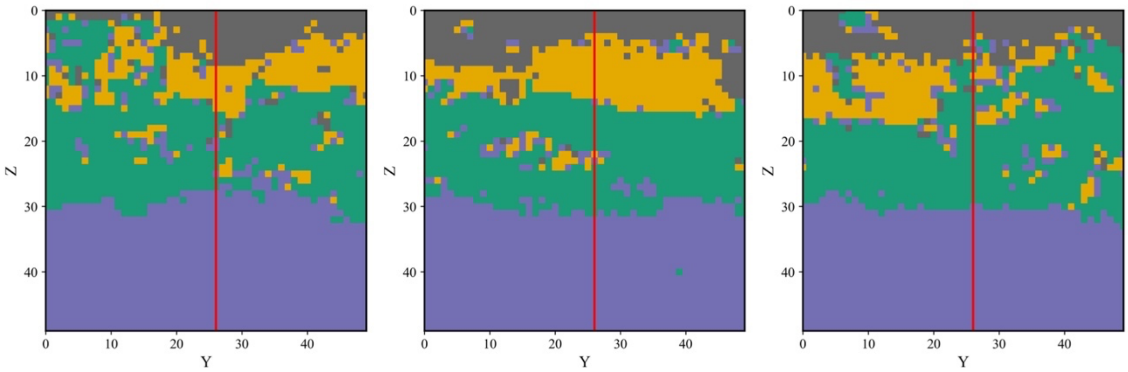

(b)

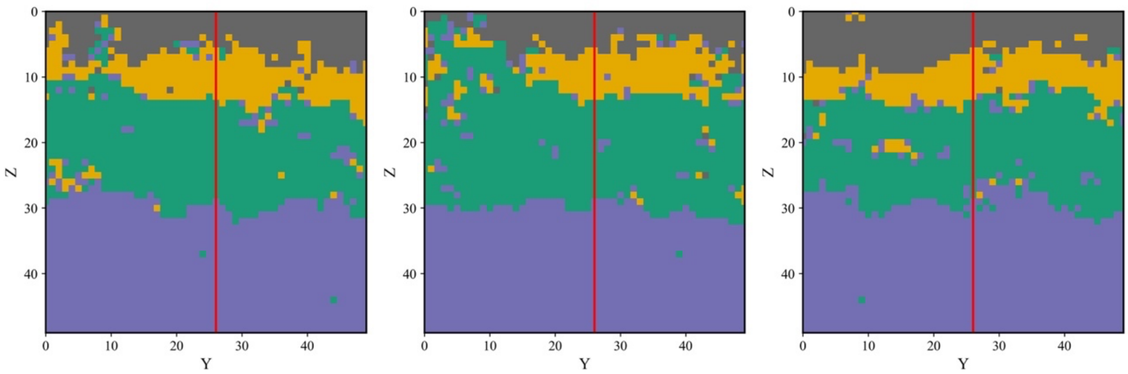

(c)

Fig. 14 Training image (a), three unconditional/random realizations (b) and three conditional/calibrated realizations (c) of the cross section at $X = 126$. The red line represents the well log location where facies are assumed to be known.

The entropy map of the cross section for 100 unconditional realizations and conditional realizations is shown in Fig. 15. As constrained by the observed data, the entropy value at the well location is 0, meaning no uncertainty.

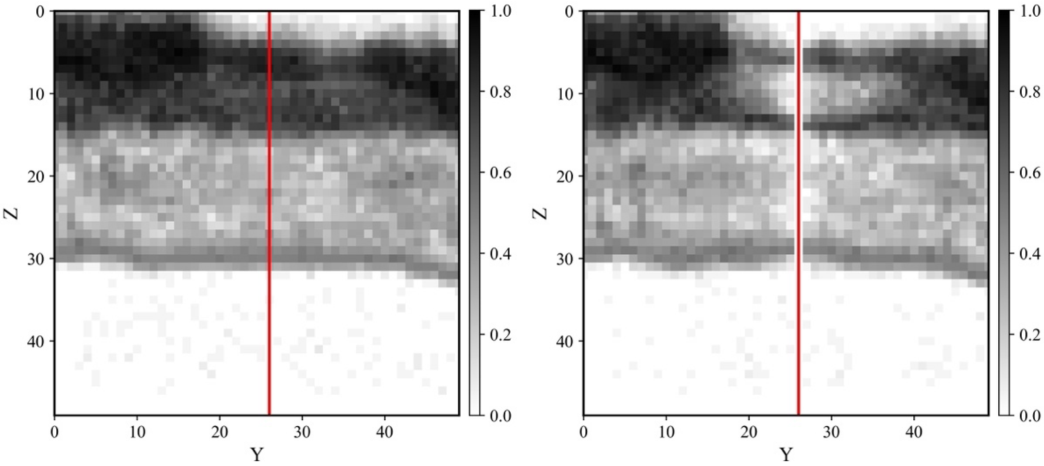

(a) (b)

Fig. 15 Entropy map of the cross section at $X = 126$ for 100 random realizations (a) and 100 calibrated realizations using GDM (b).

The MDS plot of the unconditional/random realizations and conditional/calibrated realizations is shown in Fig. 16. The training image is overlapped with the unconditional realizations and calibrated realizations in the low-dimensional space, indicating a good similarity between them.

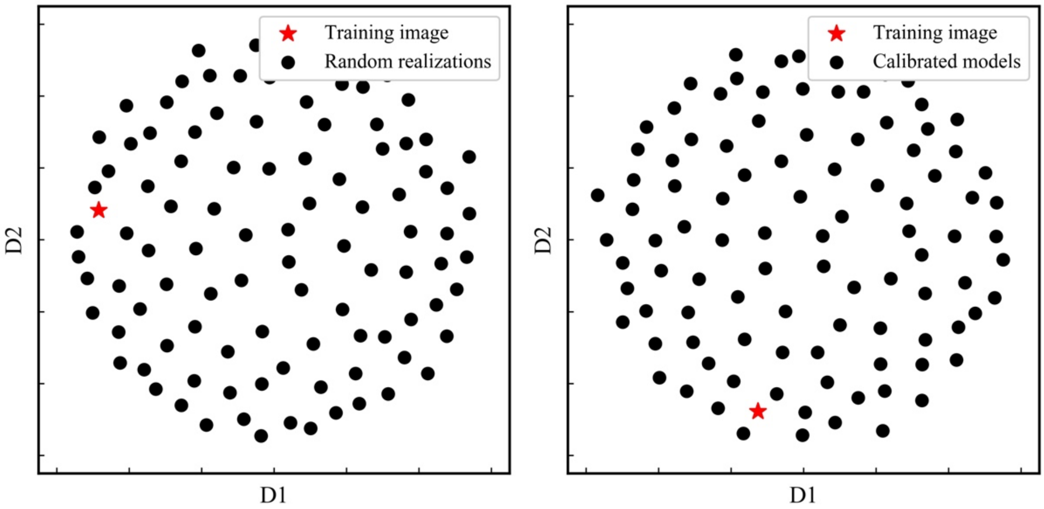

(a) (b)

Fig. 16 MDS plot of the unconditional/random realizations (a) and conditional/calibrated realizations (b), together with the training image.

The histogram of the facies proportion in displayed in Fig. 17. The unconditional/random realizations and conditional/calibrated realizations show similar facies proportions with the ones of the training image.

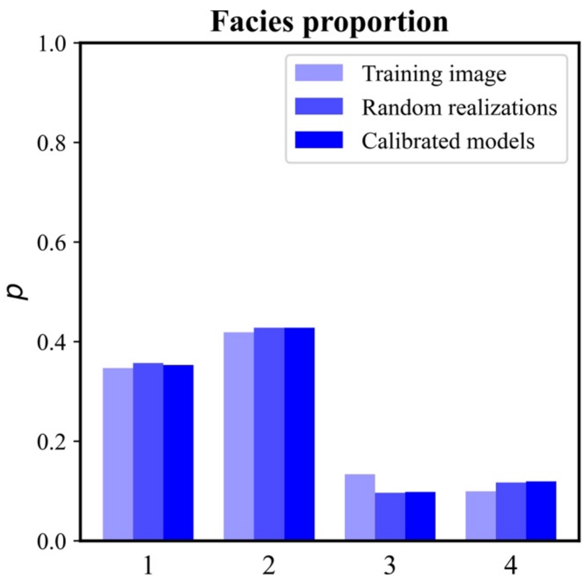

Fig. 17 Facies proportions of training image, random realizations and calibrated models.

4 Discussion

This work presents a novel approach to train generative models using a single training image, instead of a large quantity of training images required in other studies. Thus, the traditional geostatistical methods are not needed for building the training data. The proposed GANs are applied to simulate the geological facies models in 2D and 3D applications. A cutoff operation with different threshold values is applied to the output of the last layer of the generator to obtain categorical variables. In principle, the one-hot encoding scheme could be used, leading to increased computational cost. Compared to traditional geostatistical methods such as the single normal equation simulation requiring stationary training images (Strebelle, 2002), the proposed GANs can simulate more complex geological models, such as those based on geological processes without any stationary assumption. Moreover, in this study, a categorical random variable representing geological facies is applied; however, the proposed GANs can be extended to simulate continuous variables such as rock and fluid properties in subsurface models by changing the activation function in the last layer of the generator accordingly.

The gradual deformation method is applied to calibrate the random realizations generated by trained GANs to observed data, as a result of an optimization process. Compared to the unconditional realizations, the conditional/calibrated realizations by GDM can better preserve the geological structures by honoring direct measurements as shown in the presented applications (Figs. 8, 9, 14 and 15). However, conditioning/calibrating the models to observed data might require additional computational time. Alternative to the GDM, conditioning to the observed data can be directly performed in the simulation process by the trained generator, in which an extra loss function should be pre-defined to account for the content loss (Yeh et al., 2017). Moreover, the conditional probabilities or indirect measurements (i.e. soft data) can be integrated in the simulation by adopting the nu/tau model (Polyakova and Journel, 2007; Krishnan, 2008), and the softmax activation function should be used in the last layer of the generator for probabilities calculation.

5 Conclusion

We presented a new implementation of a deep learning model based on GANs to simulate geological facies models in the subsurface. Compared to other applications of the GANs on the geostatistical simulation, the proposed GANs do not require a large quantity of training data for updating neural parameters, and only one single training image is sufficient. Thus, the training of the proposed GANs does not rely on geostatistical methods to generate training data. The training image is down-sampled to different scales, and the training of GANs is performed in a multi-scale architecture, as the spatial statistical information from the training image is progressively captured. The random realizations by the trained generators are then conditioned/calibrated to observed data by gradually deforming the random noise maps using the gradual deformation method. The proposed methodology is applied for unconditional and conditional simulations to two case studies, in which a 2D river delta and a 3D aquifer analog model are successfully modelled, as shown by the MDS plot and facies proportions. The proposed methods can be extended to model continuous variables such as porosity and permeability. Future research will focus on performing hard and/or soft data conditioning in the simulation process directly with the trained generator, instead of using the gradual deformation method.

Code availability

The source code and trained model are available at https://github.com/RhFeng/SGANs

Name of Code: SGANs.

Developer: Runhai Feng.

Contact: runhai.feng@gmail.com.

Year first available: 2023.

Software: PyTorch 1.4

Program language: Python 3.6

Authorship statement

Runhai Feng developed the methodology and the code, and worked on the application; Dario Grana provided scientific advising and helped with the scientific writing.

Declaration of competing interest

The authors declare that they have no known competing financial interests or personal relationships that could have appeared to influence the work reported in this paper.

Acknowledgement

The authors acknowledge Dr. L.Y. Hu for the constructive comments and suggestions.

References

Azevedo, L., Paneiro, G., Santos, A., Soares, A., 2020. Generative adversarial network as a stochastic subsurface model reconstruction. Comput. Geosci. 24 (4): 1673–1692

Bayer, P., Comunian, A., Höyng, D., Mariethoz, G., 2015. High resolution multi-facies realizations of sedimentary reservoir and aquifer analogs. Scientific Data 2: 150033. https://doi.org/10.1038/sdata.2015.33

Caers, J., 2007. Comparing the gradual deformation with the probability perturbation method for solving inverse problems. Mathematical Geology 39: 27–52

Chan, S., Elsheikh, A.H., 2019. Parametric generation of conditional geological realizations using generative neural networks. Comput. Geosci. 23(5): 925–952

Chen, M., Wu, S., Bedle, H., Xie, P., Zhang, J., Wang, Y., 2022. Modeling of subsurface sedimentary facies using Self-Attention Generative Adversarial Networks (SAGANs). Journal of Petroleum Science and Engineering. 214: 110470

Cox, M., Cox, T., 2008. Multidimensional scaling. In: Handbook of data visualization. Springer handbooks Comp. statistics. Springer, Berlin. https://doi.org/10.1007/978-3-540-33037-0_14

Dupont, E., Zhang, T., Tilke, P., Liang, L., Bailey, W., 2018. Generating realistic geology conditioned on physical measurements with generative adversarial networks. arXiv:1802.03065

Feng, R., Grana, D., Mukerji, T., Mosegaard, K., 2022. Application of Bayesian generative adversarial networks to geological facies modeling. Mathematical Geosciences 54: 831–855

Goodfellow, I., Pouget-Abadie, J., Mirza, M., Xu, B., Warde-Farley, D., Ozair, S., Courville, A., Bengio, Y., 2014. Generative adversarial networks. arXiv:1406.2661

Hu, L.Y., 2000. Gradual deformation and iterative calibration of Gaussian-related stochastic models. Mathematical Geology 32(1): 87–108

Hu, L.Y., Blanc, G., Noetinger, B., 2001. Gradual deformation and iterative calibration of sequential simulations. Math. Geol. 33: 475–489

Hu, L.Y., Le Ravalec-Dupin, M., 2004. An improved gradual deformation method for reconciling random and gradient searches in stochastic optimizations. Math. Geol. 36(6): 703–720

Hu, L.Y., Chugunova, T., 2008. Multiple-point geostatistics for modeling subsurface heterogeneity: A comprehensive review. Water Resources Research 44: W11413

Hu, L.Y., Liu, Y., Scheepens, C., Shultz, A.W., Thompson, R.D., 2014. Multiple-point simulation with an existing reservoir model as training image. Math. Geosci. 46: 227–240

Ioffe, S., Szegedy, C., 2015. Batch normalization: accelerating deep network training by reducing internal covariate shift. arXiv: 1502.03167

Isola, P., Zhu, J.Y., Zhou, T., Efros, A.A., 2018. Image-to-image translation with conditional adversarial networks. arXiv: 1611.07004

Kingma, D.P., Ba, J., 2014. Adam: A method for stochastic optimization. arXiv: 1412.6980

Krishnan, S., 2008. The Tau model for data redundancy and information combination in earth sciences: Theory and Application. Mathematical Geosciences 40: 705–727

Laloy, E., Hérault, R., Jacques, D., Linde, N., 2018. Training-image based geostatistical inversion using a spatial generative adversarial neural network. Water Resour. Res. 54(1): 381–406

Li, C., Wand, M., 2016. Precomputed real-time texture synthesis with markovian generative adversarial networks. European Conference on Computer Vision, 702–716

Mariethoz, G., Renard, P., Straubhaar, J., 2010. The direct sampling method to perform multiple-point geostatistics simulations. Water Resources Research 46: W11536

Mariethoz, G. and Caers, J., 2014. Multiple-point geostatistics: stochastic modeling with training images. John Wiley & Sons.

Mosser, L.J., Dubrule, O., Blunt, M.J., 2018. Conditioning of three-dimensional generative adversarial networks for pore and reservoir-scale models. arXiv:1802.05622

Polyakova, E., Journel, A., 2007. The Nu expression for probabilistic data integration. Math. Geol. 39(8): 715–733

Pyrcz, M.J., Deutsch, C.V., 2014. Geostatistical reservoir modeling. Oxford university press

Shaham, T.R., Dekel, T., Michaeli, T., 2019. SinGAN: learning a generative model from a single natural image. arXiv:1905.01164v2

Shocher, A., Bagon, S., Isola, P., Irani, M., 2018. Ingan: Capturing and remapping the “DNA” of a natural image. arXiv:1812.00231

Song, S., Mukerji, T., Hou, J., 2021. Bridging the gap between geophysics and geology with generative adversarial networks. IEEE Trans Geosci Remote Sensing. https://doi.org/10.1109/TGRS.2021.3066975

Strebelle, S., 2002. Conditional simulation of complex geological structures using multiple-point statistics. Mathematical Geology 34(1): 1-21

Sun, A.Y., 2018. Discovering state-parameter mappings in subsurface models using generative adversarial networks. Geophysical Research Letters 45: 11137–11146

Sun, C., Demyanov, V., Arnold, D., 2022. Geological realism in fluvial facies modelling with GAN under variable depositional conditions. Computational Geosciences, https://doi.org/10.1007/s10596-023-10190-w

Tran, T.T., 1994. Improving variogram reproduction on dense simulation grids. Computers & Geosciences 20(7-8): 1161–1168

Yeh, R.A., Chen, C., Lim, T.Y., Schwing, A.G., Hasegawa-Johnson, M., Do, M.N., 2017. Semantic Image Inpainting with Deep Generative Models. Proceedings of the IEEE conference on computer vision and pattern recognition, 5485–5493

Zhang, C., Song, X., Azevedo, L., 2021. U-net generative adversarial network for subsurface facies modelling. Computational Geosciences 25: 553–573

Zhang, T.F., Tilke, P., Dupont, E., Zhu, L.C., Liang, L., Bailey, W., 2019. Generating geologically realistic 3D reservoir facies models using deep learning of sedimentary architecture with generative adversarial networks. Petroleum Science 16: 541–549

Zhong, Z., Sun, A.Y., Jeong, H., 2019. Predicting CO_2 plume migration in heterogeneous formations using conditional deep convolutional generative adversarial network. Water Resour. Res. 55(7): 5830–5851